Controlling the pinning time of a receding contact line under forced wetting conditions

Fernandez-Toledano, Juan-Carlos; Rigaut, Clement; Mastrangeli, Max; de Coninck, Joel

DOI
10.1016/j.jcis.2020.01.054

Publication date
2020

Document Version
Final published version

Published in
Journal of Colloid and Interface Science

Journal of Colloid and Interface Science 565 (2020) 449–457

Contents lists available at ScienceDirect

Journal of Colloid and Interface Science

journal homepage: www.elsevier.com/locate/jcis

Controlling the pinning time of a receding contact line under forced wetting conditions

J-C. Fernández-Toledano [a,*], C. Rigaut [a], M. Mastrangeli [b], J. De Coninck [a]

[a] Laboratory of Surface and Interfacial Physics (LPSI), University of Mons, 7000 Mons, Belgium
[b] Electronic Components, Technology and Materials (ECTM), Delft University of Technology, 2628CT Delft, the Netherlands

HIGHLIGHTS

- Development and validation by MD simulations of an analytical model able to predict the dynamic contact angles in a capillary liquid bridge confined between two parallel plates in relative motion with different wettabilities.
- Detailed description of the pinning/depinning process of a contact line on a chemical heterogeneity at the nanoscale.
- Development and validation by MD simulations of a geometrical model able to predict the pinning time on a chemical heterogeneity.
- The pinning time depends not only on substrate/heterogeneity wettability contrast and relative plate velocity, but also on the separation distance between the plates confining the capillary bridge.

GRAPHICAL ABSTRACT

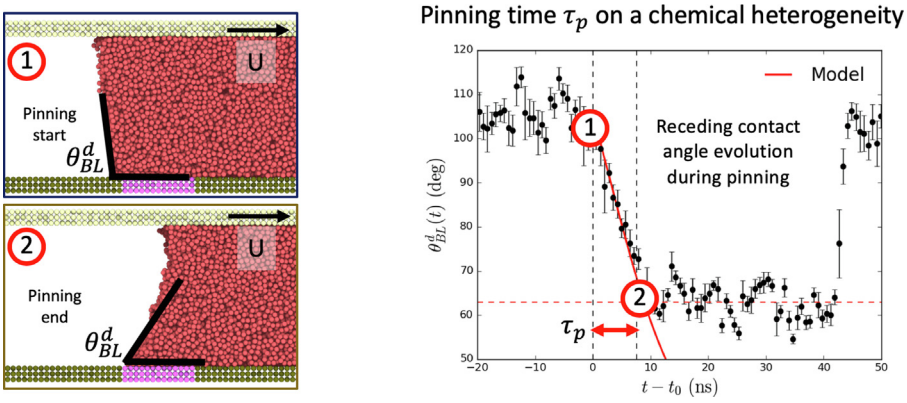

ARTICLE INFO

Article history:
Received 7 October 2019
Revised 15 January 2020
Accepted 16 January 2020
Available online 20 January 2020

Keywords:
Contact line pinning
Heterogeneous substrates
Dynamics of wetting
Molecular dynamics

ABSTRACT

Hypothesis: The contact line pinning that appears in a flow coating process over substrates patterned with chemical or physical heterogeneities has been recently applied to deposit micro- and nanoparticles with great precision. However, the mechanism underlying pinning of a receding contact line at the nanoscale is not yet well understood. In the case of a contact line pinned at a chemical heterogeneity, we hypothesise that it is possible to establish a relation between the pinning time, the contact line velocity and the liquid/plate/heterogeneity affinity that can help to optimize particle deposition.
Methods: We use large-scale molecular dynamic (MD) simulations of a finite liquid bridge formed between two parallel, non–identical, smooth solid plates. The top plate slides relative to the bottom plate inducing a displacement of the four different contact lines of the liquid bridge. The introduction of a chemical heterogeneity on the bottom plate by modifying locally the liquid–solid affinity provokes the transient pinning of the contact line in contact with the bottom substrate. By means of this simple MD simulation, we can study the mechanism of contact line pinning and its relation with the liquid/heterogeneity affinity and the contact line velocity. Additionally, we compare this mechanism with the case of the receding contact line pinned on a physical heterogeneity (a simple step discontinuity).
Findings: We propose an analytical model that predicts the values of the dynamic contact angles in the general case of a capillary liquid bridge confined between two parallel plates with different wettabilities

* Corresponding author.
E-mail address: carlos.toledano@umons.ac.be (J-C. Fernández-Toledano).

https://doi.org/10.1016/j.jcis.2020.01.054

versus the relative velocity of the top plate. These predictions are successfully validated by the results of the large–scale MD simulations. The model allows thus to predict the value of the dynamic contact angles for the different contact lines of the system versus the relative speed of the moving plate. Once the chemical heterogeneity is introduced in the bottom plate, we show that when the receding contact line reaches the patch it remains temporarily pinned while the receding contact angle evolves with time. Once the receding angle reaches the value of the equilibrium contact angle of the patch, the receding contact line overcomes pinning. A geometrical model able to predict the pinning time is proposed and validated by our MD simulations. The pinning time depends not only on the relative plate velocity and plate wettability properties but also on the separation distance between the plates confining the capillary bridge. The model can consequently be used to select the substrate wettability or meniscus geometry suitable to impose the pinning time required for specific applications.

1. Introduction

The design of regular structures by nanoparticle manipulation is a topic of major scientific and technological interest [1–3]. A particular example is provided by freeze casting, which allows to design new types of battery electrodes with superior properties [4] or to design bone scaffolds with remarkable features [5]. Another example is the attempt by many research teams to create superhydrophobic surfaces by depositing layers of nanoparticles leading to the Cassie state for sessile water drops – the well-known Lotus effect [6]. The ultimate objective of these and other methods is to use the properties of the system to self-assemble the corresponding structures. The idea is simple, but the realization is challenging. Among the available techniques, we reconsider here the flow coating method since we believe it can be considerably improved to deposit nanoparticles at will.

Forced wetting corresponds to any method by which the contact line is driven across the substrate at a steady state, as in liquid coating. Forced wetting methods have been classically used to deposit a thin liquid film of a given thickness on top of a substrate [7–10] including semiconducting polymers to create organic electronics [11]. Recently, flow coating [12] has been exploited to deposit microparticles [13,14] and nanoparticles [15,16] with great precision on relatively large substrate areas patterned with templating structures. In the technique, a confined meniscus [17] of the stabilised particle suspension is driven across a substrate having physical (topographic structures) or chemical heterogeneities (defined by a wettability contrast). The flow created by the motion of the plate and by the local evaporation of solvent confines particles in the vicinity of the receding contact line [18]. By designing physical or chemical traps on the target substrate (typically the bottom plate), it has been observed that the particles in the vicinity of the receding contact line remain trapped as a result of the balance of the particle-solid and particle-liquid interactions [19,20] as well as interfacial capillary force [12]. Under appropriate conditions in terms of sliding speed, temperature, shape of the traps and features of the nanoparticles, the deposition process can achieve high yield [16]. In both cases, the process consists of three distinct steps: (1) insertion and localization of the particle in the trap, which in the chemical heterogeneity case is triggered by the transient pinning of the receding contact line at the edge of the trap to form a liquid lens around it, whereas it can happen also before in the case of the physical heterogeneity; (2) resilience of the particle in the trap against the receding front of the meniscus and particularly the unpinning of the receding contact line; and (3) evaporative drying of the solvent in the trap, which finalizes the placement of the particle [16]. A key property of capillary assembly is the absence of deposition on the flat, homogeneous and unpatterned lyophobic surface. This ensures that the particles end up being located only within the target patterns and not elsewhere. This effect can be related to the deformation of the meniscus when it comes in contact with the edges of the traps [13,16,14].

Along with significant experimental progress in process control [14,16], some interesting advances were achieved in computational modeling of flow coating based on the Reynolds lubrication equation [21], and some theoretical predictions were obtained for the deposition of colloidal particles with this technique [22]. However, these studies are based on continuum macroscopic hydrodynamic models which require boundary conditions and which ignore the influence that the dynamics of wetting may have on the mechanism. Moreover, the contact line pinning plays a critical role in the particle deposition through the contact line and therefore, to further optimize the trapping conditions, a more comprehensive understanding of the pinning mechanism is needed. The pinning/depinning process has been previously studied for the case of drop evaporation on top of heterogeneous surfaces experimentally [23,24], computationally [25–27] and the corresponding stick times of the contact line have been successfully modelled by Shanahan et al. [28,29]. However, to the best of our knowledge, there is a lack of studies of the pinning/depinning process for contact lines formed by liquids in a capillary bridge geometry which could have many potential applications as for the particle deposition mentioned previously. Therefore, the aim of our study is to model in this geometry the transient pinning of the contact line due to the presence of heterogeneities on the substrate. We will also show that the pinning-depinning process observed in chemical traps is similar to the case of physical heterogeneities.

The present work may additionally be viewed as a generalization of previous works from our group devoted to the dynamics of wetting for a meniscus between two identical plates [30], as here we take into account the possible pinning of the receding contact line due to some heterogeneity.

The paper is organized as follows. The next section provides a description of the molecular dynamics (MD) simulation technique. In Section 3 we present an extension of our previous analytical model and its results describing a link between flow coating and dynamics of wetting. In Section 4 this model is then used to study the receding interface behavior in the presence of chemical heterogeneities on the substrate, and we detail the MD model by which we confine the moving meniscus and validate the analytical model. Section 5 discusses analogies with the behavior of receding interfaces at physical substrate heterogeneities. Discussion and further remarks are finally presented in the concluding section.

2. Molecular dynamics simulations

We study the dynamics of the three-phase contact lines formed by a liquid bridge vertically confined between two parallel, non–identical, molecularly smooth solid plates separated by a distance

H with the top plate sliding relative to the bottom plate as it is sketched in Fig. 1. Full details of the simulation methods, base parameters and potentials were presented in our previous publications on droplet spreading [31], capillary bridges [30,32] and the wetting of nanofibers [33]. To recapitulate, all atoms interact among them with a Lennard-Jones (LJ) potential:

$$V(r_{ij}) = 4\epsilon C_{AB}\left(\left(\frac{a}{r_{ij}}\right)^{12} - \left(\frac{a}{r_{ij}}\right)^{6}\right) \quad (1)$$

Here r_{ij} is the distance between the atoms i and j. The coupling parameter C_{AB} tunes the affinities between the different types of atoms: liquid–liquid (L-L), solid–solid (S-S) and solid–liquid (S-L). The ϵ and a parameters are the depth of the potential well and an effective atomic diameter, respectively. For both solid and liquid atoms we use $a = 0.35$ nm and $\epsilon = k_B T$, where k_B is the Boltzmann constant and $T = 33$ K is the temperature. We fix to 1 the coupling between the L–L and the S–S interactions ($C_{LL} = C_{SS} = 1$) and it is varied independently being $C_{S_tL} = 0.8$ for the interaction top plate/liquid and $C_{S_bL} = 0.6$ bottom plate/liquid. The selection of the solid/liquid couplings determines the value of the equilibrium contact angle of the liquid on the top plate ($\theta_t^0 = 78.0^\circ \pm 2.0^\circ$) and on the bottom plate ($\theta_b^0 = 107.1^\circ \pm 3.2^\circ$). We introduce a standard cut-off for the LJ interaction of $r_c = 2.5a$ and then, the pair potential is set to zero for $r_{ij} = 2.5a$.

Each solid plate contains 39000 atoms in a rectangular square-planar lattice arrangement containing three atomic layers. The equilibrium distance between atoms interacting through the Lennard-Jones potential ($2^{1/6}a = 0.393$ nm) is used as the lattice parameter. The atoms can vibrate thermally from their initial positions r_0 to an instantaneous location r according to the harmonic potential $V_h(r) = 100\epsilon|r - r_0|^2/a^2$.

We model the presence of a chemical heterogeneity on the bottom plate as a patch of length L_p larger than the amplitude of the contact line fluctuation (typically between 2 and 3 nm for our system [30,34]). Two different patch lengths have been considered, $L_p = 4.7$ nm and 9.4 nm. The y and z dimensions of the patch are identical to the plate. The chosen y dimension implies that all the points of the contact line reach the boundary between plate and the patch at the same time and due to the periodical boundary condition in the y axis, the patch is effectively infinite in this direction. Although this approximation should be valid for most experimental situations, it could be interesting in future work to investigate what changes when considering finite heterogeneities. The equilibrium contact angle between the liquid and the patch θ_p^0 is determined by the coupling C_{S_pL}. Three patch couplings were studied, $C_{S_pL} = 0.8$, 0.9 and 1.0 corresponding to $\theta_p^0 = (107.1 \pm 3.2)^\circ, (69.8 \pm 3.2)^\circ$ and $(54.1 \pm 3.1)^\circ$, respectively.

The liquid contains 8928 molecular linear chains of 8 atoms each (71424 atoms in total). The adjacent atoms in a molecule are bonded through a FENE potential $V_F(r) = -0.5\kappa R_0^2 \ln[1 - (r/R_0)^2]$ where r is the distance between the atoms, $\kappa = 12.25\epsilon/a^2$ and $R_0 = 1.4a$ is the maximum extension length. All atoms have a mass equal to carbon atoms (12 g/mol).

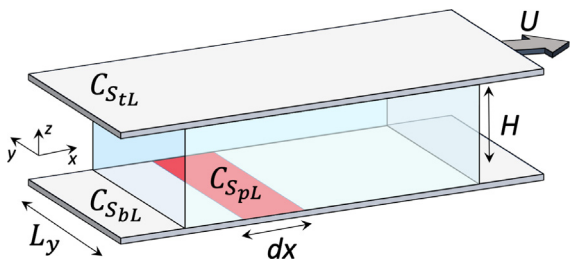

Fig. 1. Sketch of the system under study, composed of two solid plates separated by a distance H with the top plate sliding at a speed U relative to the bottom plate. The case of a chemical heterogeneity in the bottom plate is also illustrated.

The dimensions of the simulation box are $(L_x, L_y, L_z) = (98.2, 10.2, 13.9)$ nm. We set periodic boundary conditions in the x and y directions. In order to analyze the effect of the selected geometry on the results, two different gaps between the plates were studied: $H = 10.2$ and 20.4 nm. The time step used to integrate the Newton equations is 0.005 ps. Classical methods [35] were used to determine the surface tension between the liquid and its vapor phase $\gamma_L = (2.84 \pm 0.56)$ mN/m and its shear viscosity $\eta_L = (0.264 \pm 0.005)$ mPa·s. This uncomplicated model includes all the fundamental elements necessary to describe the details of the flow coating technique [16]. The aim here is not to reproduce all the complexity of a real experiment but to discriminate the mechanism controlling wetting and the contact line pinning in flow coating experiments.

At the start of each simulation, the liquid bridge is equilibrated between the plates for 2×10^6 time steps with a thermostat using a velocity rescaling applied to the liquid and the solid phases. This time is sufficient to achieve an equilibrated system characterized by stable values of energies and density profiles. Then, we apply the thermostat only on the plates to mimic a real experiment and we move the top plate at constant velocity from 1 to 5 m/s. Next, we determine the four contact-line positions and their corresponding contact angles as follows. First, we locate the position of the meniscus by subdividing the liquid in several layers and then fitting the corresponding shapes with a sector of a circle. The circular approximation of the local meniscus shape is legitimate since we do not account for gravity in the model, given that the characteristic size of the S-L interface is far smaller than the capillary length $L_C = \sqrt{\gamma_L/\rho g} \approx 798$ μm. The intersection of the fitted circle with the plate determines the contact-line location and its tangent at this intersection provide us the value of the contact angle. This technique works well for plates with the same wettability. For plates with different wettabilities, it still works for the system at equilibrium. However under dynamic conditions, as in the present study, two circles are needed to fit the meniscus profile and obtain the contact angles. In this case, the profile is cut in two and the circles are fitted individually on the half-interfaces. We have checked that when the plates are not moving, we recover the same results versus the solid–liquid interaction as in [30].

3. Homogeneous substrates

In a previous publication, Blake et al. [30]we have considered the dynamics of wetting of a bridge of the same liquid as used in the present work and confined between two identical parallel plates moving in opposite directions at constant velocity U. In this case, once the system reaches the stationary regime, the mean location of the contact lines does not change with time. The authors observed that the velocity of the first layer of liquid in contact with the plate U_{1L} in the centre of the contact area was lower than the plate velocity U due to the presence of slip between the liquid and the solid phases. The first layer of liquid is here defined as the molecules confined between the plate and the first minimum in the density due to layering [31]. The associated slip velocity at the contact line, $U_s^{cl} = U - U_{1L}$, modifies the dynamics of wetting of the system, i.e. the relation between the dynamic contact angles and the contact-line velocity U_{CL}. The low surface tension of the liquid and the considered values of the plate velocities lead to a linear relation between the out-of-balance capillary force $\gamma_L(\cos\theta^0 - \cos\theta^d)$ and the contact-line velocity U_{CL} [30]:

$$\zeta U_{CL} - \zeta U_s^{cl} = \gamma_L\left(\cos\theta^0 - \cos\theta^d\right) \tag{2}$$

where $\zeta = k_B T/k^0\lambda^3$ is the contact-line friction where λ and k^0 are the jump length and the jump frequency, respectively. This relationship can be viewed as a linear approximation of the full Molecular Kinetic Theory [30]:

$$\zeta U_{CL} - \zeta U_s^{cl} = \frac{2k_BT}{\lambda^2}\sinh\left[\frac{\lambda^2\gamma\left(\cos\theta^0 - \cos\theta^d\right)}{2k_BT}\right] \tag{3}$$

The linear approximation in Eq. (2) is valid whenever the argument of the hyperbolic sine in Eq. (3) is lower than 0.1 as in our case due to the low value of the surface tension.

The liquid velocity at the centre of the solid–liquid interface has a linear relation with the plate velocity, $U_{1L} = \alpha U$. Then, the slip at the centre of the solid–liquid interface is just $U_s^c = U_{1L} - U = (\alpha - 1)U$. However, at the contact line we have an additional contribution to the slip coming from the decay of the liquid velocity in contact with the plate since this velocity is varying from a constant value at the centre of the S-L interface to zero at the contact line. Then, at the contact line $U_s^{cl} = U_{1L}/2 - U$. By knowing the contact-line friction ζ and the slip given by the parameter α it is thus possible to measure the contact-line friction by fitting the data in the range of plate velocities where the linear approximation given in Eq. (2) holds. This friction ζ was shown to be identical to the one obtained from spontaneous spreading simulations where slip is absent.[31] The results are reproduced in Table 1.

In the present work we extend the theory to model flow coating as a liquid bridge confined between two parallel, *non-identical* plates where only the top plate moves at constant velocity U as sketched in Fig. 2a. Accordingly, the affinity between the top plate and the liquid (characterized by a coupling C_{S_tL}) and the affinity between the bottom plate and the liquid (characterized by a coupling C_{S_bL}) will, in general, be different. Also, the top (ζ_t) and the bottom (ζ_b) contact line friction coefficients, as well as the top and the bottom slip (determined by α_t and α_b respectively) may be different. In this geometry, when the system reaches the stationary regime, the contact lines will move at constant velocity $U_{CL} = -U/2$. To mimic the geometry of Ref. [30] and to measure the velocities with respect to the contact-line location, we can change the original frame of reference, in which the top plate is moving at velocity U and the bottom plate is at rest as represented in Fig. 2a (framework 1), to a reference system in which the contact lines are not moving shown in Fig. 2b (framework 2) by subtracting the contact-line velocity from all the atoms of the system. The contact-line velocity in framework 1 will just be

$$U_{CL} = \frac{U}{2} + (\alpha_t - \alpha_b)\frac{U}{2} \tag{4}$$

Then, the top plate and the bottom plate velocities in framework 2 will be $U - U_{CL}$ and $-U_{CL}$, respectively. Therefore, we can identify the velocity of the first layer of liquid close to each plate in the framework 2 as

Table 1
Equilibrium contact angles θ^0 and values of contact-line friction ζ (from Ref. [31]).

C_{SL}	θ^0 (deg)	ζ (mPa·s)	α
0.4	126.0 ± 1.1	0.09 ± 0.04	0.50 ± 0.05
0.5	118.1 ± 2.8	0.21 ± 0.06	0.44 ± 0.05
0.6	107.1 ± 3.2	0.31 ± 0.10	0.64 ± 0.06
0.7	96.5 ± 3.2	0.56 ± 0.12	0.69 ± 0.05
0.8	78.9 ± 2.0	0.77 ± 0.14	0.81 ± 0.06
0.9	69.8 ± 3.2	0.95 ± 0.20	0.85 ± 0.07
1.0	54.1 ± 3.1	1.05 ± 0.23	0.90 ± 0.06

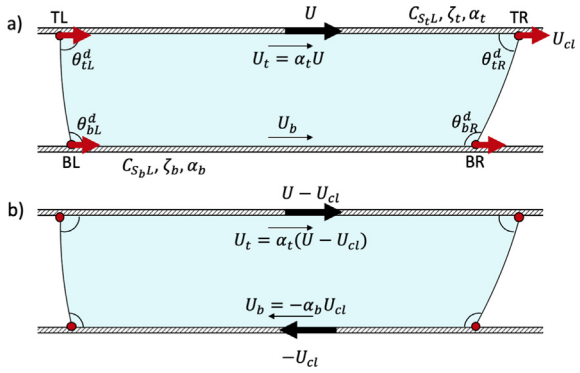

Fig. 2. (a) Framework of reference 1 where the top plate moves at constant velocity U and the bottom plate remains at rest. Here, the four contact lines move at constant velocity U_{cl}. (b) Framework of reference 2 where the four contact lines remain at rest and the top and bottom plates move at constant velocity of $U - U_{cl}$ and $-U_{cl}$, respectively.

$$U_t = \alpha_t(U - U_{CL}) \tag{5}$$

$$U_b = -\alpha_b U_{CL} \tag{6}$$

We can thus generalize Eq. (2) to this system:

$$\zeta_t U_{CL} - \zeta_t U_{s,t}^{cl} = \gamma_L\left(\cos\theta_t^0 - \cos\theta_t^d\right) \tag{7}$$

$$\zeta_b U_{CL} - \zeta_b U_{s,b}^{cl} = \gamma_L\left(\cos\theta_b^0 - \cos\theta_b^d\right) \tag{8}$$

where $U_{s,t}^{cl}$ and $U_{s,b}^{cl}$ are the slip velocity at the contact line on the top and on the bottom plate, respectively.

With this simple model we can then compute the value of the four different dynamic contact angles ($\theta^d_{bL}, \theta^d_{bR}, \theta^d_{tL}$ and θ^d_{tR} showed in Fig. 2a) and the liquid velocities in proximity of each plate by knowing the surface tension γ_L, the equilibrium contact angle of the bottom and top plates (θ_b^0 and θ_t^0), the contact-line friction coefficients for the bottom and the top plate (ζ_b and ζ_t), the slip parameters (α_b and α_t) and the velocity of the top plate U.

To check the validity of the model, we selected $C_{S_tL} = 0.8$ and $C_{S_bL} = 0.6$ as the couplings for the top and the bottom plate, respectively, and we moved the top plate at velocity U between 1 to 5 m/s. The contact-line frictions ζ_t and ζ_b as well as the slip factors are given in Table 1. The measured contact line velocity U_{cl} for the different plate velocities U are shown in Fig. 3a together with the predicted values according with Eq. (4). Fig. 3b shows the calculated values of U_t and U_b measured with respect to the contact-line location (framework 2) as well as the prediction given by Eqs. (5)–(4). Very good agreement between theory and simulation is observed. Fig. 3c shows the dynamic (advancing and receding) contact angle on the bottom (θ_b^d) and on the top (θ_t^d) plate for different plate velocities and the predicted values from Eqs. (7) and (8). Clearly, the model reproduces the simulation data reasonably well within the errorbars.

In real experiments [15,16], various factors including the inevitable presence of heterogeneities on the plates make the slip negligible, and hence $\alpha_t = \alpha_b = 1$. In this case, the equation for the receding contact angle on the bottom plate simplifies to:

$$\cos\theta_b^d = \frac{\zeta_b}{\gamma_L}\frac{U}{2} + \cos\theta_b^0 \tag{9}$$

where the key parameter is clearly the contact-line friction on the bottom plate ζ_b. Although it has been derived for a nanometric system, Eq. (9) can be also applied to macroscopic systems for a range of contact line velocities where the linear approximation between

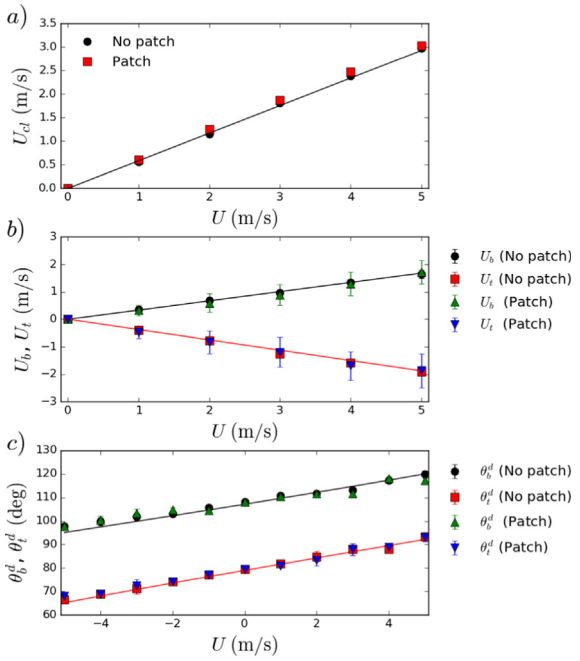

Fig. 3. (a) Contact line velocity measured for the different velocities of the plate (symbols) and the prediction from Eq. (4) (line). (b) Velocity of the first layer of liquid in contact with the top (U_t) and the bottom (U_b) plates and the prediction from Eqs. (5)–(4). (c) Dynamic contact angles on the bottom (θ_b^t) and on the top (θ_t^d) plates and the model predictions from Eqs. (7) and (8). All three figures correspond to $C_{S_bL} = 0.6$ and $C_{S_tL} = 0.8$, and to homogeneous bottom plate (No patch) or presence of heterogeneity on the bottom plate far from the contact lines (Patch) where noted.

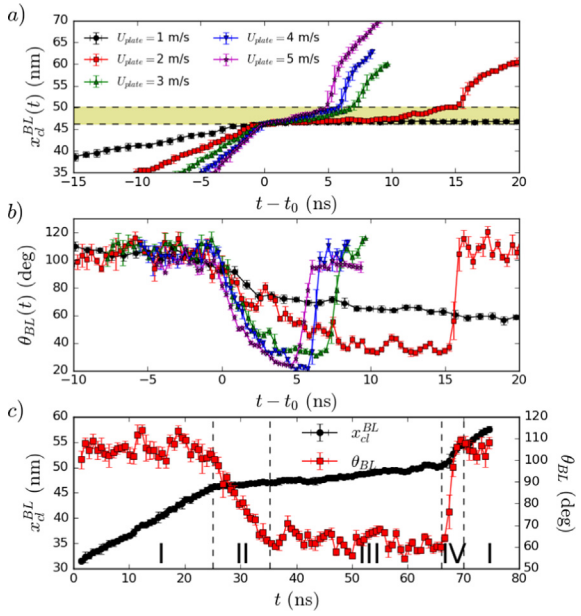

Fig. 4. (a) Evolution of the receding contact line location on the bottom plate (BL) for $C_{S_pL} = 1.0$ and different plate velocities U. (b) Evolution of the receding contact angle on the bottom plate $\theta_{BL}(t)$ for $C_{S_pL} = 1.0$ and the same velocities as in subplot (a). (c) Evolution of the contact line location and the contact angle for the BL contact line for $C_{S_pL} = 0.9$ and $U = 1$ m/s. The different regions are delimited by vertical dashed lines.

the capilary force and the contact line velocity is valid. The prediction of the receding angle is a key point to understand wetting dynamics implications in contact line pinning as developed in the next section.

4. Chemical heterogeneities

When a contact line is moving on top of a substrate, the presence of heterogeneities in the substrate will affect the wetting dynamic of the system and therefore, the contact line velocity [19,12,16,18,13,20]. Here we focus on the study of chemical heterogeneities defined by a wettability contrast.

Initially the patch is located at the centre along x of the solid/liquid interface and the system is equilibrated with the thermostat applied to all atoms of the system. Then, we remove the scaling of the velocity over the liquid atoms and the thermostat is only applied on the solid atoms. This allows some dissipation of energy between the liquid and the solid as in real experiments. The top plate is moved at constant velocity U and the contact lines start to move. When the system reaches the stationary regime, the four contact lines move at constant velocity given by Eq. (4). After some time, the receding contact line of the bottom plate reaches the patch and the contact line remains pinned from a finite time interval which depends on the plate velocity, the wettability contrast between the bottom plate and the patch and, as we will show later, on the plate separation H.

Fig. 4a shows the evolution of (a) the receding contact line location on the bottom plate x_{BL} (marked as BL in Fig. 2a) close to the location of the heterogeneity and (b) its corresponding dynamic contact angle θ_{BL} for $C_{S_pL} = 1.0$ for different velocities of the top plate U. In order to compare the effect of U we set the time origin at t_0 defined as the instant where x_{BL} reaches the heterogeneity. We can observe the presence of four different regions in the evolution of x_{BL} and θ_{BL} strongly influenced by the top plate velocity. To observe the correlation between the changes of x_{BL} and θ_{BL}, we present both in the same plot in Fig. 4c for $C_{S_pL} = 0.9$ and $U = 1$ m/s. Region I extends until x_{BL} reaches the heterogeneity represented as a colored horizontal band in Fig. 4a. Here, the contact line moves with a velocity given by Eq. (4). The corresponding dynamic contact angles for $t < t_0$ in Fig. 4b can also be predicted by Eqs. (7) and (8) as shown in Fig. 3. Therefore, the presence of one small chemically heterogeneous patch on the bottom plate does not modify the wetting dynamics outside of the patch which can be described with the model proposed in the previous section.

Once x_{BL} reaches the patch we have region II where the bottom left (BL) contact line (see Fig. 2a) dramatically decreases its velocity (pinning). The presence of this second region is more evident at low velocities. For example, in Fig. 4a the contact line remains stuck for $U = 1$ m/s for the whole considered period of time and x_{BL} moves very slowly for $U = 2$ m/s until $t - t_0 = 9$ ns. In this region II the dynamic contact angle θ_{BL} decreases from its initial value of region I until it reaches the equilibrium contact angle of the patch θ_p^0 which defines then the starting of the region III. This confirms that the depinning of the receding contact line originates from the dynamics of the process: for a given speed, the fact that the contact line does not have the appropriate contact angle to cross the patch forces it to slow down until the contact angle has been able to evolve and reach the right value. In region III θ_{BL} evolves from θ_p^0 to a steady value and afterwards it remains constant. Meanwhile, x_{BL} moves much faster than in region II (depinning) and eventually it reaches the end of the heterogeneity which delimits the end of region III and the starting point of the final region IV. In this region IV the contact line rapidly recoils to recover the receding contact angle outside the patch θ_{BL}. Hence a much faster contact line velocity is observed when the contact line escapes from the patch. Finally, after region IV the contact line recovers the dynamic angle and the velocity of region I.

In this work, we focus on the analysis of the displacement of the BL contact line only (see Fig. 2a). Nevertheless, the evolution of the other three contact lines is identical to that of the BL contact line in

all regions except region II. In region II the BL contact line remains pinned and the other three contact lines move at the same velocity related to the variation of the BL contact angle and under the constraint of conservation of liquid volume.

The regions showed in Fig. 4c are quite similar to the regions reported in the study of the pinning/depinning mechanism of the contact line during droplet evaporation. In their pioneering work, Picknett and Bexon [36] identified two regimes in droplets evaporation on smooth substrates: the constant contact radius region (CCR) where the contact line is pinned to the solid substrate (similar to our region II) and the constant contact angle region (CCA) where the contact angle remains constant while the contact line recedes (similar to our region III). More recent works have extended this study to the analysis of the pinning-depinning transition (CCR-CCA transition) that appears in spontaneous drop evaporation on substrates patterned with a series of hydrophobic and hydrophilic stripes [25,26,37]. There, the contact line moves along the hydrophobic stripe during the evaporation (equivalent to our region I). After some time, the contact line reaches the hydrophobic-hydrophilic boundary and it remains pinned while the contact angle changes (CCR equivalent to our region II) although the observation at the nanoscale of this region suggests that, at the molecular level, pinning is actually a strong decrease in the contact line velocity and not an absence of displacement as already described in literature [37]. When the contact angle reaches a critical value, the contact line continues receding across the hydrophilic patch and the contact angle eventually reaches a constant value (CCA equivalent to our region III). When the contact line reaches the hydrophilic-hydrophobic boundary there is a sudden jump of the contact line due to the unbalance of Young's force [26] corresponding to our region IV. Obviously, the displacement of the top plate, or equivalently, the dynamics of wetting associated to flow coating, allows to control in great details the different mechanisms appearing when the receding interface has to cross the patch. Let us now consider in details each of these regions.

4.1. Region II

Once the BL contact line reaches the heterogeneity region II starts where the contact line drastically reduces its velocity (quasi–pinning) and the associated contact angle $\theta_{BL}(t)$ decreases with time which is very similar to the "Constant Contact Radius" (CCR) region observed in the modeling of drop evaporation over a patterned substrate [25,26,37] characterized by a constant value of the contact radius and a variation of the contact angle. The length of this time period is characterized by the pinning time τ_p defined as the time required for the receding contact angle on the bottom plate to evolve from its stationary value in the absence of the patch θ_b^{st} to the equilibrium contact angle of the liquid on the patch θ_p^0 as represented in Fig. 4c. Once $\theta_{BL}(t) \approx \theta_p^0$, the BL contact line increases its velocity and the depinning occurs (see Fig. 4c). This angle transition can be modelled geometrically if we simplify the problem considering that the BL contact line remains totally pinned in this region and that the change of the contact angle θ_{BL} can be linked to the displacement of the top plate as sketched in Fig. 5a. If we neglect the presence of slip as expected in real experiments, we can approximate the velocity of the advancing contact line on the top plate as $U_{cl} \approx U/2$ and then, the evolution of the BL contact angle in the region II can be modelled as:

$$\frac{U}{2}t \approx H\left(\cot\theta_{BL}(t) - \cot\theta_b^{st}\right) \tag{10}$$

Then,

$$\theta_{BL}(t) \approx \arctan\left(\frac{1}{\cot\theta_b^{st} + \frac{U}{2H}t}\right) \tag{11}$$

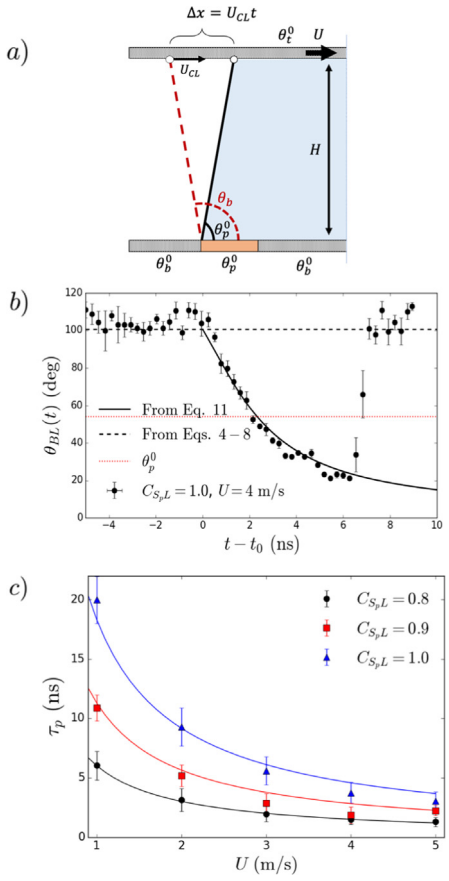

Fig. 5. (a) Sketch for the geometrical approximation used to determine the pinning time. The red dashed line represents the initial interface when the contact line pins and the black line is the interface when the contact line deepens. (b) Evolution of $\theta_{BL}(t)$ for $C_{S_pL} = 1.0$ and $U = 4$ m/s and the prediction from Eq. (11). The dotted line corresponds to θ_p^0. (c) Pinning time τ_p for some performed simulations (symbols) and the corresponding estimations from Eq. (12). (For interpretation of the references to colour in this figure legend, the reader is referred to the web version of this article.)

Fig. 5b shows the time evolution of θ_{BL} for $C_{S_pL} = 1.0$ and $U = 4$ m/s, the initial value of the contact angle in region I predicted from Eqs. (4)–(8) (dashed line) and the time evolution of θ_{BL} inside region II predicted from Eq. (11).

It is then straightforward to estimate the pinning time from Eq. (10) considering $\theta_{BL}(\tau_p) = \theta_p^0$:

$$\tau_p \approx \frac{2H}{U}\left(\cot\theta_p^0 - \cot\theta_b^{st}\right) \tag{12}$$

Then, by increasing the difference in wettability between the bottom substrate and the patch (for example by using a superhydrophic substrate) the pinning time will increase. Introducing the natural time unit $\tau_0 = H/U$, we obtain a dimensionless equation which should be valid for any liquid meniscus between two plates in the linear approximation:

$$\frac{\tau_p}{\tau_0} = 2\left(\cot\theta_p^0 - \cot\theta_b^{st}\right) \tag{13}$$

where θ_b^{st} can be estimated from Eq. (9) for velocities where there is a linear dependence between U and the capillary force. This is always the case in our simulations.

Fig. 5c shows the pinning time versus the plate velocity obtained from the simulations for the different patches (wettabilities) and the prediction given by Eq. (12). Clearly, the agreement is very good.

One important prediction derived from this simple model is that the pinning time depends not only on the plate velocity U and on the wettabilities of the plate but also on the geometry, i.e. on the separation distance between the plates H. In order to check this relation between τ_p and H, we run simulations with a double separation $H_2 = 2H = 20.4$ nm. Fig. 6a shows the evolution of θ_{BL} for $C_{S_pL} = 1.0, U = 3$ m/s for both plate separations and the expected values obtained from Eq. (11) which successfully predicts the strong influence of H on pinning time. As a corroboration of the influence of H on the pinning, we present in Fig. 6b the pinning time for $C_{S_pL} = 0.8$ and the different plate velocities for both plate separations and the prediction computed from Eq. (12). Clearly, this simple model is able to capture reasonably well the values of the pinning time as well as the influence of the plate separation.

The pinning behavior of the receding contact line observed in the MD simulations and captured in the extended analytical model presented above is consistent with experimental characterizations of meniscus geometry, deformation and dynamics in flow coating over heterogeneous substrates [17,38]. Notably, the extent of contact line pinning is known to be modulated by the thickness of the meniscus (i.e., the distance between the confining plates H), since the latter is one of the parameters that controls the macroscopic stiffness of the meniscus: a thicker meniscus is a more compliant meniscus, and thus susceptible to larger elongation of the receding interface upon pinning of the receding contact line [17]. Unpinning is then regularly observed to be followed by contact line recoil, as also seen in the MD model. More generally and with respect to applications in particle deposition from suspensions, contact line pinning is *de facto* exploited to deform the receding meniscus interface, with important and convenient effects over local solvent evaporation flux and consequent particle accumulation [13,16].

4.2. Region III

Once θ_{BL} reaches the value of the equilibrium contact angle of the heterogeneity θ_p^0, the BL contact line increases drastically its velocity which corresponds to the depinning transition. It is tempting to identify this region III as the "Constant Contact Angle" (CCA) region observed in the modeling of drop evaporation over a patterned substrate [25,26,37] characterized by a constant value of the contact angle and a variation of the contact line position. The classical method to model this phenomenon corresponds to a quasi-static process where the contact line velocity does not affect the value of the contact angles. However, in the dynamic process presented in this work the role of the contact line velocity cannot be neglected and the dynamics of wetting should be taken into account in this region. Therefore, region III is not a constant contact angle region. The presence of a flow inside the liquid introduces an additional force contribution at the contact line which modifies the associated force balance. To overcome this additional force, the contact angle at the contact line has to change from its equilibrium value to a dynamical one [39]. Therefore, the evolution of $\theta_{BL}(t)$ initiated in region II does not stop when the bottom receding contact angle θ_{BL} reaches the equilibrium contact angle of the patch θ_p^0. $\theta_{BL}(t)$ will overcome θ_p^0 and will continue to decrease until it reaches some critical value θ_p^d and then, the corresponding unbalanced Young's force $\gamma(\cos\theta_p^0 - \cos\theta_p^d)$ will compensate the additional force contribution at the contact line introduced by the presence of the flow.

To estimate the dynamic contact angle of the BL contact line moving on top of the heterogeneity we use the set of Eqs. (7) and (8) to predict the velocity of the first layer of liquid in contact with the bottom plate U_b. Then, we extract the dynamic contact angle from the linear version of the MKT of a contact line moving on top of the patch

$$\zeta_p U_{1L} = \gamma(\cos\theta_p^0 - \cos\theta_p^d) \tag{14}$$

where ζ_p is the contact line friction of the heterogeneity that is showed in Table 1 for each coupling C_{S_pL}. Fig. 7a shows the measured contact angle on the patch and the results using Eq. (14).

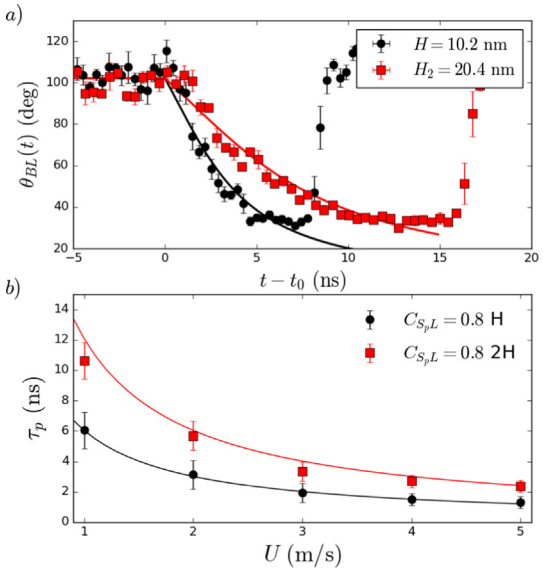

Fig. 6. (a) Evolution of $\theta_{BL}(t)$ for $C_{S_pL} = 1.0$ and $U = 3$ m/s for both plate separations. The lines correspond to the estimation from Eq. (11). (b) Pinning time versus plate velocity for $C_{S_pL} = 0.8$ and both plate separations. The lines corresponds to the predictions from Eq. (12).

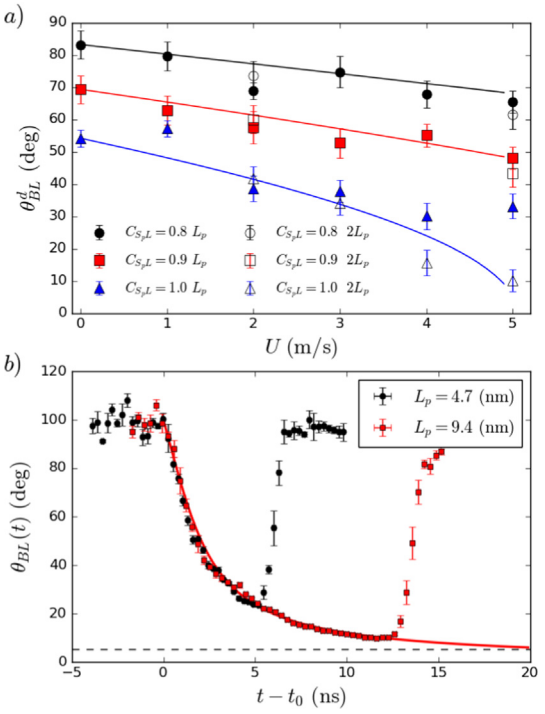

Fig. 7. (a) Contact angle of the BL contact line in region III before escape from the patch for the different simulations performed. The full and open symbols correspond to the smaller and the larger L_p, respectively. The lines corresponds with the results from Eq. (14). (b) Evolution of $\theta_{BL}(t)$ for $C_{S_pL} = 1.0, U = 5$ m/s and both patch lengths L_p. The continuous line corresponds with the results from Eq. (11).

The model predicts quite well the simulations results except for $C_{S_pL} = 1.0$ at the larger velocity $U = 5$ m/s. To understand this discrepancy we have run additional simulations where we doubled the length of the heterogeneity in x, i.e. $L_p = 9.4$ nm. Fig. 7b shows the evolution of $\theta_{BL}(t)$ for $C_{S_pL} = 1.0$ and $U = 5$ m/s for the two lengths of the patch. We observe that both curves initially overlaps but for the shorter patch, the contact line is able to escape from the heterogeneity before it reaches the steady state. Then, the dynamic angle in region III is larger than the one expected for this velocity of the BL contact line. However, the larger patch is long enough for θ_{BL} to reach the steady value. Therefore, the length of the patch in x does not affect the pinning time τ_p but it could affect the minimum value of the contact angle of the BL contact line. If the length of the patch is short enough, the BL contact line will escape from the patch before reaching the steady state. The values of the final dynamic angles in region III for different C_{S_pL} and U for the longer L_p are showed as open symbols in Fig. 7a. As it can be seen, we have differences only for $C_{S_pL} = 1.0$ and when the plate is large enough, the measured values coincide with the predicted values from Eq. (14).

5. Similarities with physical heterogeneities

When the receding contact line reaches a physical heterogeneity on the bottom plate, similar pinning dynamics is induced as in the case of a chemical patch. To show this, we run additional simulations using a model including a step discontinuity on the bottom plate to represent a physical heterogeneity. As sketched in Fig. 8a, the step is characterized by a sharp edge at the frontier among the two separations $H_1 = 10.2$ nm and $H_2 = 20$ nm between the bottom and the top plate. Initially, this edge is located at the centre of the liquid meniscus. By moving the top plate at constant velocity U a flow is generated within the liquid and, as in the case of the chemical heterogeneity, the contact line moves at constant velocity U_{CL} until the receding contact line in contact with the bottom plate reaches the edge. The process occurring at the physical heterogeneity then follows a similar dynamics to the one seen with the chemical heterogeneity. In this case, the meniscus is pinned at the edge of the step in the bottom plate, as shown in Fig. 8b. The shape of the interface is modified by the movement of the top plate which leads to a change of the contact angle as shown in Fig. 8c. Once this angle reaches the equilibrium value for the vertical part of the edge, the contact line unpins and moves downward over the vertical interface (not shown). The abrupt jump in the contact angle value at the end of the pinning apparent in Fig. 8c is due only to the change of the reference plane for contact angle measurement from the horizontal to the vertical. The behaviour of the receding contact line in the presence of an edge is captured by the so-called Gibbs' criterion and widely observed experimentally [40,41].

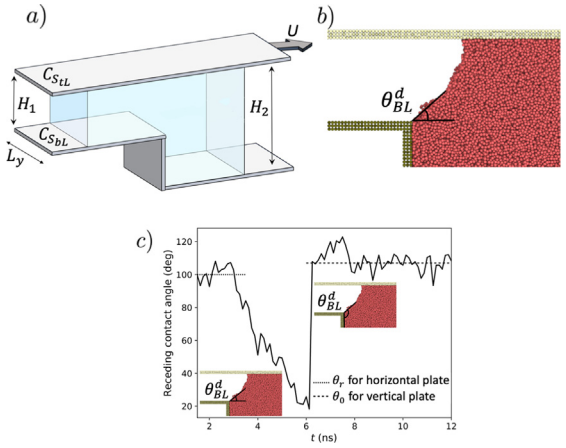

Fig. 8. (a) Scheme of the physical heterogeneity. (b) Snapshot of a simulation with the receding contact line pinned at the physical heterogeneity. (c) Evolution of the contact angle on the edge. The lines at the left and the right side represent respectively the receding contact angle for the horizontal plate and the equilibrium contact angle for the vertical edge.

The prediction of variable settling time of the contact line at the edge of the heterogeneity as a function of the sliding speed inferred from the model has direct implications for the understanding of capillary particle deposition by flow coating. We can for instance expect the settling time to directly affect the accumulation of particles in proximity of the receding contact line, as the transient deformation of the meniscus influences the local solvent evaporation flux and hence the convective flow dragging the particles towards the receding front. Moreover, longer settling times – and more generally, slower sliding speeds – correlate experimentally with higher particle assembly yield in topographical traps [13].

6. Conclusions

We have performed large-scale molecular dynamics simulations to analyze at the molecular scale the mechanism underlying pinning–depinning transition of a receding contact line on patterned substrates under forced wetting conditions. Initially, we have studied a liquid bridge confined between two homogeneous parallel plates with different wetabilities when the top plate is moving at constant velocity U_{plate} with respect the bottom one. As an extension of our previous work [30] where we modelled the wetting dynamics in the case of identical plates, here we have presented an improved and more general model containing different affinities between the liquid and the top/bottom plates. The predictions of this model for the values of the advancing and receding contact angles in both plates as a function of U_{plate} have been successfully compared with the results of MD simulations.

We have then modelled a patch of chemical heterogeneities on the bottom plate by modifying locally the liquid–solid affinity. We have shown that when the receding contact line reaches the patch it remains pinned while the receding contact angle evolves with time. Once the receding angle reaches the value of the equilibrium contact angle of the patch, the receding contact line will overcome the pinning. We have proposed a geometrical model able to predict the pinning time which depends not only on the velocity and the wettability properties but also on the separation distance between the plates of the capillary bridge. We have corroborated this dependence by running additional simulations with larger plate separation whose pinning time can be successfully reproduced with the proposed model.

One of the outcomes of this paper is that, for the first time to the best of our knowledge, we have demonstrated the dynamic origin of contact line depinning in a capillary bridge geometry. This mechanism leads to a predictable pinning time as described in Eq. (12). This model can now be used to link the liquid-patch affinity or the plate separation distance with any time of pinning required by some application. In fact, according with the proposed model, the pinning time can be controlled just by tunning the separation between the plates. This geometical dependence of the pinning time differs from the experimental [23,24], computational [25–27] and theoretical [28,29] pinning time obtained for pinning–depinning transitions observed for sesile drop. If this result can be validated experimentally, this will be the first step to significantly improve applications such as the deposition of nanoparticles at the receding contact line during pinning.

It would now be interesting to explore experimentally the implications of the proposed relations for particle assembly yield

and other aspects of the forced wetting process. Importantly, our simulation model does not yet take into account the full complexity of the process, and in particular the evaporation at the contact line, which depends on the local contact angle and plays a crucial role in capillary particle assembly [13]. Also, the periodical boundary condition along the y axis in the MD model implies that the patch is effectively infinite in this direction. Although this approximation should be valid for most experimental situations, it could be interesting to investigate what changes when we consider finite size heterogeneities. These aspects will be included in a future version of the model.

Declaration of Competing Interest

The authors declare that they have no known competing financial interests or personal relationships that could have appeared to influence the work reported in this paper.

Acknowledgments

The authors would like to thank Terence D. Blake for many useful inputs and valuable comments. This research was partially funded by UMONS. The authors thank the European Space Agency (ESA) and the Belgian Federal Science Policy Oce (BELSPO) for their support in the framework of the PRODEX Programme. Computational resources have been provided by the Consortium des Equipements de Calcul Intensif (CECI), funded by the Fonds de la Recherche Scientifique de Belgique (F.R.S.-FNRS) under Grant No. 2.5020.11.

References

[1] Z. Nie, A. Petukhova, E. Kumacheva, Properties and emerging applications of self-assembled structures made from inorganic nanoparticles, Nat. Nanotechnol. 5 (2010) 15–25.
[2] P. Marchetti, M. Mechelhoff, A.G. Livingston, Tunable-porosity membranes from discrete nanoparticles, Scient. Rep., vol. 5.
[3] S.J. Tan, M.J. Campolongo, D. Luo, W. Cheng, Building plasmonic nanostructures with DNA, Nat. Nanotechnol. 6 (2011) 268–276.
[4] H. Bai, Y. Chen, B. Delattre, A.P. Tomsia, R.O. Ritchie, Bioinspired large-scale aligned porous materials assembled with dual temperature gradients, Sci. Adv. 1 (2015) e1500849.
[5] B. Delattre, R. Amin, J. Sander, J. De Coninck, A.P. Tomsia, Y.-M. Chiang, Impact of Pore Tortuosity on Electrode Kinetics in Lithium Battery Electrodes: Study in Directionally Freeze-Cast $LiNi_{0.8}$ $Co_{0.15}$ $Al_{0.05}$ O_2 (NCA), J. Electrochem. Soc. 165 (2018) A388–A395.
[6] E. Celia, T. Darmanin, E. Taffin de Givenchy, S. Amigoni, F. Guittard, Recent advances in designing superhydrophobic surfaces, J. Colloid Interface Sci. 402 (2013) 1–18.
[7] B.G. Prevo, D.M. Kuncicky, O.D. Velev, Engineered deposition of coatings from nano- and micro-particles: a brief review of convective assembly at high volume fraction, Colloids Surf. A: Physicochem. Eng. Aspects 311 (2007) 2–10.
[8] W. Han, Z. Lin, Learning from coffee rings: ordered structures enabled by controlled evaporative self-assembly, Angew. Chem. Int. Ed. 51 (2012) 1534–1546.
[9] L. Li, M.H. Köpf, S.V. Gurevich, R. Friedrich, L. Chi, Structure formation by dynamic self-assembly, Small 8 (2012) 488–503.
[10] T. Kraus, D. Brodoceanu, N. Pazos-Perez, A. Fery, Colloidal surface assemblies: nanotechnology meets bioinspiration, Adv. Funct. Mater. 23 (2013) 4529–4541.
[11] X. Gu, L. Shaw, K. Gu, M.F. Toney, Z. Bao, The meniscus-guided deposition of semiconducting polymers, Nat. Commun. 9 (2018) 534.
[12] Y. Cui, M.T. Björk, J.A. Liddle, C. Sönnichsen, B. Boussert, A.P. Alivisatos, Integration of colloidal nanocrystals into lithographically patterned devices, Nano Lett. 4 (2004) 1093–1098.
[13] L. Malaquin, T. Kraus, H. Schmid, E. Delamarche, H. Wolf, Controlled particle placement through convective and capillary assembly, Langmuir 23 (2007) 11513–11521.
[14] S. Ni, L. Isa, H. Wolf, Capillary assembly as a tool for the heterogeneous integration of micro-and nanoscale objects, Soft Matter 14 (2018) 2978–2995.
[15] T. Kraus, L. Malaquin, H. Schmid, W. Riess, N.D. Spencer, H. Wolf, Nanoparticle printing with single-particle resolution, Nat. Nanotechnol. 2 (2007) 570.
[16] V. Flauraud, M. Mastrangeli, G.D. Bernasconi, J. Butet, D.T.L. Alexander, E. Shahrabi, O.J.F. Martin, J. Brugger, Nanoscale topographical control of capillary assembly of nanoparticles, Nat. Nanotechnol. 12 (2016) 73–80.
[17] P. Born, S. Blum, A. Munoz, T. Kraus, Role of the meniscus shape in large-area convective particle assembly, Langmuir 27 (2011) 8621–8633.
[18] C. Kuemin, L. Nowack, L. Bozano, N.D. Spencer, H. Wolf, Oriented assembly of gold nanorods on the single-particle level, Adv. Funct. Mater. 22 (2012) 702–708.
[19] R. Ashkar, M.J.A. Hore, X. Ye, B. Natarajan, N.J. Greybush, T. Lam, C.R. Kagan, C. B. Murray, Rapid large-scale assembly and pattern transfer of one-dimensional gold nanorod superstructures, ACS Appl. Mater. Interfaces 9 (2017) 25513–25521.
[20] D. Nepal, M.S. Onses, K. Park, M. Jespersen, C.J. Thode, P.F. Nealey, R.A. Vaia, Control over position, orientation, and spacing of arrays of gold nanorods using chemically nanopatterned surfaces and tailored particle-particle-surface interactions, ACS Nano 6 (2012) 5693–5701.
[21] D.S. Hariprasad, G. Grau, P.R. Schunk, K. Tjiptowidjojo, A computational model for doctoring fluid films in gravure printing, J. Appl. Phys., vol. 119, 13.
[22] F. Doumenc, J.-B. Salmon, B. Guerrier, Modeling flow coating of colloidal dispersions in the evaporative regime: prediction of deposit thickness, Langmuir 32 (51) (2016) 13657–13668.
[23] E. Bormashenko, A. Musin, M. Zinigrad, Evaporation of droplets on strongly and weakly pinning surfaces and dynamics of the triple line, Colloids Surf. A: Physicochem. Eng. Aspects 385 (2011) 235–240.
[24] B. Sobac, D. Brutin, Triple-line behavior and wettability controlled by nanocoated substrates: influence on sessile drop evaporation, Langmuir 27 (2011) 14999–15007.
[25] F.-C. Wang, H.-A. Wu, Pinning and depinning mechanism of the contact line during evaporation of nano-droplets sessile on textured surfaces, Soft Matter 9 (2013) 5703.
[26] Q. Li, P. Zhou, H.J. Yan, Pinning-depinning mechanism of the contact line during evaporation on chemically patterned surfaces: a lattice boltzmann study, Langmuir 32 (2016) 9389–9396.
[27] A. Mazloomi Moqaddam, D. Derome, J. Carmeliet, Dynamics of contact line pinning and depinning of droplets evaporating on microribs, Langmuir 34 (2018) 5635–5645.
[28] M.E.R. Shanahan, Simple theory of stick-slip wetting hysteresis, Langmuir 11 (1995) 1041–1043.
[29] M. Shanahan, K. Sefiane, Kinetics of Triple Line Motion during Evaporation, Wettability and Adhesion, vol. 6, Leiden, Koninklijke Brill NV, 2009, pp. 19–31.
[30] T.D. Blake, J.-C. Fernandez-Toledano, G. Doyen, J. De Coninck, Forced wetting and hydrodynamic assist, Phys. Fluids 27 (2015) 112101.
[31] E. Bertrand, T.D. Blake, J.D. Coninck, Influence of solid-liquid interactions on dynamic wetting: a molecular dynamics study, J. Phys.: Condens. Matter 21 (2009) 464124.
[32] J.C. Fernandez-Toledano, T.D. Blake, P. Lambert, J. De Coninck, On the cohesion of fluids and their adhesion to solids: Young's equation at the atomic scale, Adv. Colloid Interface Sci. 245 (2017) 102–107.
[33] D. Seveno, T.D. Blake, J. De Coninck, Young's equation at the nanoscale, Phys. Rev. Lett. 111 (2013) 1–4.
[34] J.-C. Fernández-toledano, T. Blake, J. De Coninck, Contact-line fluctuations and dynamic wetting, J. Colloid Interface Sci. 540 (2019) 322–329.
[35] M. Allen, D. Tildesley, Computer Simulation of Liquids, Clarendon Pr, Oxford, 1987.
[36] R. Picknett, R. Bexon, The evaporation of sessile or pendant drops in still air, J. Colloid Interface Sci. 61 (1977) 336–350.
[37] J. Zhang, H. Huang, X.-Y. Lu, Pinning-depinning mechanism of the contact line during evaporation of nanodroplets on heated heterogeneous surfaces: a molecular dynamics simulation, Langmuir 35 (2019) 6356–6366.
[38] C.L. Wirth, M. De Volder, J. Vermant, Fabrication of planar colloidal clusters with template-assisted interfacial assembly, Langmuir 31 (2015) 1632–1640.
[39] J.-C. Fernandez-Toledano, T.D. Blake, J. De Coninck, Youngs equation for a two-liquid system on the nanomete, Langmuir 33 (2017) 2929–2938.
[40] F.-M. Chang, S.-J. Hong, Y.-J. Sheng, H.-K. Tsao, Wetting invasion and retreat across a corner boundary, J. Phys. Chem. C 114 (2010) 1615–1621.
[41] W.-J.A. de Wijs, J. Laven, G. de With, Wetting forces and meniscus pinning at geometrical edges, AIChE J. 62 (2016) 4453–4465.